ADVANCED THEORY AND SIMULATIONS
www.advtheorysimul.com

Understanding Robustness of Magnetically Driven Helical Propulsion in Viscous Fluids Using Sensitivity Analysis

*Roberto Venezian and Islam S. M. Khalil**

Magnetically-actuated helical microrobots can propel themselves in fluids and tissues-like mediums with a wide range of Reynolds numbers (*Re*). The properties of physiological fluids and input parameters vary in time and space and have a direct influence on their locomotion along prescribed paths. Therefore, understanding the response of microrobots to variations in rheological properties and input parameters become increasingly important to translate them into in vivo applications. Here, a physical framework is presented to understand and predict key parameters whose uncertainty affect certain state variables most. A six-degree-of-freedom magneto-hydrodynamic model is developed based on the resistive force theory (RFT) to predict the response of robots swimming through different fluids and examine their response during transitions into Newtonian–viscoelastic interfaces. Performance of the robot, while swimming in a fluid with a fixed viscosity, is quantified using sensitivity analysis based on the magneto-hydrodynamic model. The numerical results show how abrupt changes in viscosity can affect their ability to rotate with the rotating field in synchrony. The sensitivity analysis shows that the states of the robot are mostly sensitive to variations in the actuation frequency. Open-loop experiments are performed using a permanent-magnet robotic system comprising a robotic arm and a rotating permanent magnet to actuate and control a helical robot at the Newtonian–Viscoelastic interface and validate the theoretical predictions of the RFT-based sensitivity analysis.

1. Introduction

Over the past decades, manmade microrobots have been designed and developed to move in a variety of ways under the influence of an external stimulus to perform certain tasks in a tetherless fashion. In particular, the use of untethered microrobots in medical applications is a promising method for targeting hard-to-reach locations and for their potential impact in minimally invasive medicine.[1–5] These microdevices hold promise to reduce the invasiveness of surgical treatments and their effectiveness has been investigated to perform a wide range of non-trivial tasks such as biopsy,[6,7] drug delivery,[8–10] diagnostic sensing,[11,12] revasculatization of clogged vessels,[13] and cell transplantation.[14] These tasks have been executed using functionalized microstructures mostly in the shape of a helix or a filament driven by external stimuli. Magnetically driven helical microrobots are one of the most promising designs for in vivo applications since they can swim under the influence of a relatively weak time-periodic magnetic field in the millitesla range (<10 mT) which is harmless to cells and tissues.[15] Furthermore, this combination of design and power source has been adopted to perform motion in Newtonian and viscoelastic mediums for a wide range of Reynolds numbers (*Re*), thus increasing their potential range of applications.

The magnetic actuation of helical microrobots can be implemented by applying uniform or nonuniform fields generated using electromagnetic and permanent-magnet systems.[16–18] The first method uses configurations of electromagnetic coils that are powered independently such that their superimposed field exerts a magnetic torque to align and rotate the helical microrobot. The second method makes use of rotating permanent magnet (RPM) that are position controlled using serial link manipulators. Fountain et al. have addressed the use of RPM to actuate helical bodies in a fluid characterized by low-*Re* ($Re < 10^{-1}$),[19] to increase the size of the workspace that is most likely to be limited by the configuration of electromagnets. They have studied two fundamental control strategies for a single RPM actuator: axial control, with the microrobot located along the rotation axis of the magnet, and radial control with the microrobot positioned perpendicular to the magnet. Despite the intrinsic inhomogeneities of the controlled fields that are generated using these systems, the relatively large workspace and the open-configuration make them desirable in wireless actuation of magnetic microrobots. It has also been demonstrated that combining multiple RPMs can

R. Venezian, I. S. M. Khalil
Department of Biomechanical Engineering
Faculty of Engineering Technology
University of Twente
Enschede 7500 AE, The Netherlands
E-mail: i.s.m.khalil@utwente.nl

The ORCID identification number(s) for the author(s) of this article can be found under https://doi.org/10.1002/adts.202100519

DOI: 10.1002/adts.202100519

generate time-periodic fields that are more uniform, thereby increasing the size of the gradient-free workspace.[20]

Once equipped with an external stimulus, the response of helical robots can be predicted using hydrodynamic models to estimate the time-dependent velocities of the swimmers and the fluids. Rondeborn et al.[21] have experimentally tested the resistive force theory (RFT)[22] on macroscopic swimmers in silicone oil by tuning geometric parameters of the helix, and compared measurements to numerical results. Lin et al. have theoretically studied and optimized the swimming performance of double curved conical microhelical robots and presented optimal geometric parameters (helicity angle, helical length, helical wire diameter, cone angle, and the number of threads) in terms of swimming speed.[23] Tabak has implemented an RFT-based model for helical swimmers and validated the theoretical predictions with experiments. The proposed strategy improves the RFT-based analysis by the incorporation of correction coefficients based on hydrodynamic impedance analysis of the time-dependent solution of Navier–Stokes equations. The motion in a confined environment (lumen) filled with glycerin has been predicted by the model and the step-out frequency has been also estimated.[24] Additionally, a control technique has been defined to account for the flow near the boundaries of the lumen by modifying the resistance matrix; incorporating an additional stiffness correction factor. Recently, Tang et al. have wirelessly controlled nanorobots and demonstrated precise maneuvers within complex in vitro and in vivo environments, and investigated their kinetic behavior based on the geometric properties of their body and the effects imparted by nearby solid boundaries.[25] Khalil et al. have utilized a permanent-magnet robotic system consisting of two synchronized RPMs that are able to achieve gradient-free region within the workspace of the system and control a helical microrobot while approaching and rubbing a blood clot.[13] They have used the RFT to predict the response of helical robots in a confined environment filled with biological fluids and the removal rate of unwanted cells using an in vitro thrombus model. Gómez et al. have characterized the motion of helical swimmers in well-characterized shear-thinning inelastic fluids, and observed that the swimming speed scales linearly with the actuation frequency similar to that of a Newtonian fluid.[26] They have concluded that the swimming speed increase originates from confinement-like effect due to viscosity stratification and not a direct consequence of a local decrease of the flow viscosity around the helical swimmers.

The complexities of physiological fluids (different flow patterns, near wall effects,[27] heterogeneous rheological properties, and concentrated cells[28]) poses some challenges to translate in vitro experimentation into in vivo applications. Untethered devices are likely required to perform motion in environments with heterogeneous rheological and structural properties, in which the local forces vary in time and space based on the biological composition of fluids and stiffness of soft tissues.[29] The heterogeneous structural properties of the environment can also be a direct consequence of the interface between two mediums like Netwonian–viscoelastic interface. Such interface is likely to require the helical robot to maintain a swimming behavior along a prescribed path or a straight-run trajectory toward a target. Thus, it is necessary to understand the influence of variations in the surrounding environment to develop robust locomotion strategies in an open-loop environment. Consequently, the hydrodynamics of helical robots must be investigated over a range of rheological properties theoretically and experimentally, and the ability of helical swimmers to drill through these interfaces must be addressed.

In this paper, a 6-degrees-of-freedom (6-DOF) RFT-based magneto-hydrodynamic model is presented to simulate the motion of helical robots in heterogeneous viscous fluid with space-varying viscosity. The relative importance of each input parameter (actuation frequency and relative distance between the helical robot and the actuating magnet) is quantified using global sensitivity analysis. Furthermore, a permanent-magnet robotic system consisting of a serial manipulator with an RPM attached to its end-effector is used to validate the numerical results in an open-loop fashion. The experimental setup is used to demonstrate the ability of helical robots to drill through the Newtonian–viscoelastic interface between mediums, while the numerical results aim to define control strategies to robustly control helical robots for space-varying rheological properties.

2. Modeling of Helical Propulsion and Magnetic Actuation

Consider a helical robot of diameter d_r, length L, and magnetic dipole moment $\boldsymbol{m}_r \in \mathbb{R}^{3\times1}$, moving under the influence of a time-periodic magnetic field $\boldsymbol{B}(\boldsymbol{p}) \in \mathbb{R}^{3\times1}$ inside a medium with variable viscosity η characterized by Reynolds number $Re = \rho_f U_r L/\eta$, where ρ_f is the density of the medium and U_r is the swimming speed of the robot. The robot is actuated such that it transitions from low-viscosity to high-viscosity fluids with ratio of $\eta_0 = \eta_2/\eta_1$, where η_1 and η_2 are the low- and high-viscosity of the fluid, respectively, as shown in **Figure 1**a. It is also possible to predict the behavior of the robot between Newtonian and viscoelastic medium, in a manner analogous to the variable viscosity case. In this case, the second medium can be considered as a non-Newtonian medium with elastic modulus E. Prediction of the hydrodynamic response when the robot transitions between the fluids involves modeling of magnetic and hydrodynamic forces and torques in 3D space.

2.1. Magnetic Actuation of the Helical Robot

The magnetic force and torque, generated at the position of the helical robot $\boldsymbol{p} \in \mathbb{R}^{3\times1}$ from the field source, depend on the magnetic flux density $\boldsymbol{B}(\boldsymbol{p})$ and the magnetic dipole of the microrobot $\boldsymbol{m}_r$ as follows

$$\begin{pmatrix} \boldsymbol{F}_m \\ \boldsymbol{\tau}_m \end{pmatrix} = \begin{pmatrix} (\boldsymbol{m}_r \cdot \nabla)\boldsymbol{B}(\boldsymbol{p}) \\ \boldsymbol{m}_r \times \boldsymbol{B}(\boldsymbol{p}) \end{pmatrix} \tag{1}$$

where $\boldsymbol{F}_m \in \mathbb{R}^{3\times1}$ and $\boldsymbol{\tau}_m \in \mathbb{R}^{3\times1}$ are magnetic forces and torques, respectively. The magnetic flux density can be accurately modeled using the magnetic dipole approximation,[30] such that

$$\boldsymbol{B}(\boldsymbol{p}) = \frac{\mu_0}{4\pi\|\boldsymbol{p}\|^3}\left(3\hat{\boldsymbol{p}}\hat{\boldsymbol{p}}^T - \mathbb{I}\right)\boldsymbol{M}_{act} = \frac{\mu_0}{4\pi\|\boldsymbol{p}\|^3}\mathbb{H}\boldsymbol{M}_{act} \tag{2}$$

where $\mu_0 = 4\pi \times 10^{-7}$ N A^{-2} is the permeability of free space, $\boldsymbol{p}$ is the vector from the center of the field source and position of

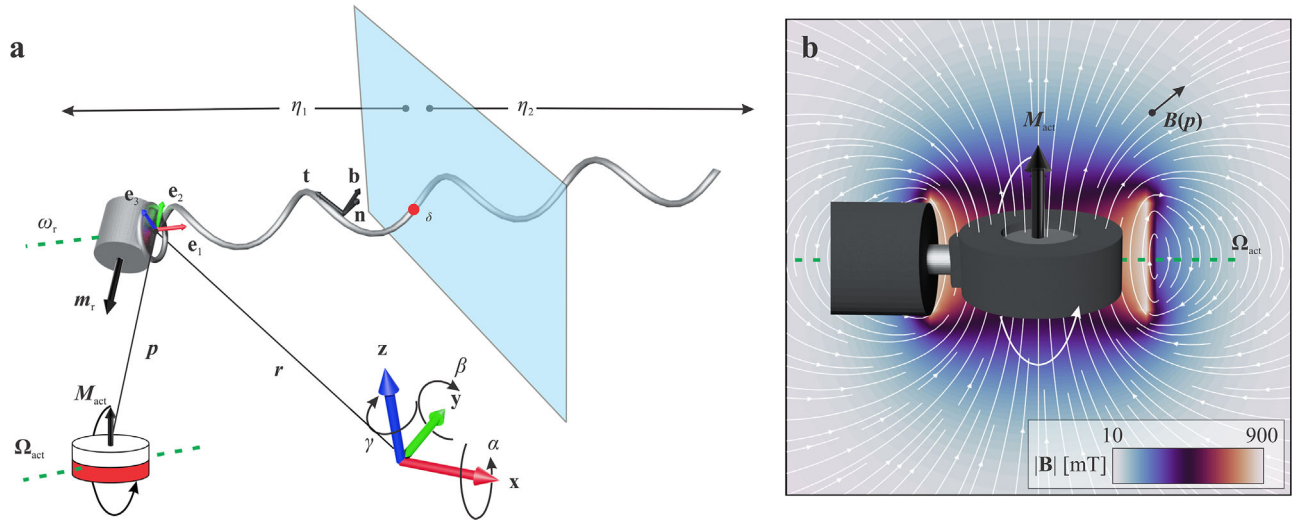

Figure 1. Helical propulsion works by rotating a helix about its long axis using an external magnetic field. a) Kinematics of the helical body is described using the moving Frenet–Serret frame, {**t**, **n**, **b**}, along the arc length, with respect to a material frame of reference $\{\mathbf{e}_1, \mathbf{e}_2, \mathbf{e}_3\}$. Position and orientation of the helical robot are represented by $\boldsymbol{r}$ and (α, β, and γ) with respect to a reference frame {**x**,**y**,**z**}. The transparent plane represents an imaginary interface between low-viscosity (η_1) and high-viscosity (η_2) mediums or Netwonian–viscoelastic interface. b) The external magnetic field is produced using a rotating permanent magnet (RPM) fixed to a robotic manipulator to control the direction of its magnetic dipole moment, $\boldsymbol{M}_{act}$. The axis of rotation of the RPM, $\hat{\boldsymbol{\Omega}}_{act}$, and the long axis of the helical robot, $\hat{\boldsymbol{\omega}}_h$, are coupled and enable helical propulsion.

the helical robot, $\boldsymbol{M}_{act} \in \mathbb{R}^{3\times1}$ A m^2 is the dipole moment of the actuator magnet and $\mathbb{I} \in \mathbb{R}^{3\times3}$ is the identity matrix. This expression gives an effective method to generate the desired field $\boldsymbol{B}(\boldsymbol{p})$ at a distance $\boldsymbol{p}$ by controlling the actuator magnet's pose $\boldsymbol{M}_{act}$, as shown in Figure 1b. Furthermore, the position-dependent matrix $\mathbb{H} \in \mathbb{R}^{3\times3}$ defines the mapping between the rotation axis $\hat{\boldsymbol{\Omega}}_{act}$ of an RPM and the axis of rotation of the magnetic field $\hat{\boldsymbol{\omega}}_h$ at a point $\boldsymbol{p}$. Mahoney and Abbott have developed a control strategy to actuate untethered magnetic devices using a single RPM.[31] These methods are based on the point dipole model presented in Equation (2). Given the rotation axis of the RPM, it is possible to calculate the axis of rotation of the magnetic field, and vice versa, we have

$$\hat{\boldsymbol{\Omega}}_{act} = \widehat{\mathbb{H}\hat{\boldsymbol{\omega}}_h}, \quad \text{and} \quad \hat{\boldsymbol{\omega}}_h = \widehat{\mathbb{H}^{-1}\hat{\boldsymbol{\Omega}}_{act}} \tag{3}$$

This actuation strategy allows steering of helical robots by controlling the rotation axis of the actuator magnet $\hat{\boldsymbol{\Omega}}_{act}$, and in this case the viscous drag force and torque must balance the magnetic force and torque to complete the dynamics.

2.2. Helical Propulsion through Newtonian–Viscoelastic Interface

In low-*Re*, the inertial forces are negligible and the response of the helical robot to an externally applied magnetic field is governed by the balance between magnetic, viscous drag, and gravitational forces and torques, thus we have

$$\begin{pmatrix} \boldsymbol{F}_m + \boldsymbol{F}_g + \boldsymbol{F}_{visc} \\ \boldsymbol{\tau}_m + \boldsymbol{\tau}_g + \boldsymbol{\tau}_{visc} \end{pmatrix} = 0 \tag{4}$$

where $\boldsymbol{F}_{visc} \in \mathbb{R}^{3\times1}$ and $\boldsymbol{\tau}_{visc} \in \mathbb{R}^{3\times1}$ are the viscous drag force and torque, respectively. Further, $\boldsymbol{F}_g \in \mathbb{R}^{3\times1}$ and $\boldsymbol{\tau}_g \in \mathbb{R}^{3\times1}$ are the force and torque exerted on the robot due to gravity and are given by

$$\begin{pmatrix} \boldsymbol{F}_g \\ \boldsymbol{\tau}_g \end{pmatrix} = \begin{pmatrix} V(\rho_r - \rho_f)\mathbf{R}_{Lab}^T \boldsymbol{g} \\ (\boldsymbol{r}_{CoV} - \boldsymbol{r}_{CoM}) \times \boldsymbol{F}_g \end{pmatrix} \tag{5}$$

where V is the volume of the swimmer, ρ_r and ρ_f are the density of the swimmer and the fluid in which the microrobot swims, respectively. The vectors $\boldsymbol{r}_{CoV} \in \mathbb{R}^{3\times1}$ and $\boldsymbol{r}_{CoM} \in \mathbb{R}^{3\times1}$ describe the position of the center of volume (CoV) and center of mass (CoM) of the swimmer, while $\boldsymbol{g} \in \mathbb{R}^{3\times1}$ is a vector representing gravitational acceleration and $\mathbf{R}_{Lab} \in \mathbb{R}^{3\times3}$ is the time-dependent rotation matrix between the material frame of reference of the robot, $\{\mathbf{e}_1, \mathbf{e}_2, \mathbf{e}_3\}$, and a fixed frame of reference, as shown in Figure 1a. The rotation matrix $\mathbf{R}_{Lab}$ is obtained by quaternion integration as the robot experiences complex rigid-body rotations.[32] One direct consequence of the negligible inertia force is that the hydrodynamics of the helical body is linear. Therefore, the viscous drag on the magnetic robot is calculated based on the RFT as follows[32]

$$\begin{pmatrix} \boldsymbol{F}_{visc} \\ \boldsymbol{\tau}_{visc} \end{pmatrix} = -\left(\int_0^{\ell} \begin{bmatrix} \mathbf{R}\mathbf{C}\mathbf{R}^T & -\mathbf{R}\mathbf{C}\mathbf{R}^T\mathbf{S}_{tail} \\ \mathbf{S}_{tail}\mathbf{R}\mathbf{C}\mathbf{R}^T & -\mathbf{S}_{tail}\mathbf{R}\mathbf{C}\mathbf{R}^T\mathbf{S}_{tail} \end{bmatrix} ds + \begin{bmatrix} \mathbf{A} & \mathbf{B} \\ \mathbf{B}^T & \mathbf{D} \end{bmatrix} \right) \begin{pmatrix} \boldsymbol{U}_r \\ \boldsymbol{\omega}_r \end{pmatrix} \tag{6}$$

where ℓ is the counter length of the tail, $\boldsymbol{U}_r \in \mathbb{R}^{3\times1}$ and $\boldsymbol{\omega}_r \in \mathbb{R}^{3\times1}$ are the rigid-body linear and angular swimming velocity vectors of the robot, respectively. Further, $\mathbf{R} \in \mathbb{R}^{3\times3}$ is the rotation matrix between local Frenet–Serret frames and the reference frame of the robot, and $\mathbf{S}_{tail} \in \mathbb{R}^{3\times3}$ is the local cross-product that couples linear translation to rotation. The viscous drag coefficient matrix $\mathbf{C} \in \mathbb{R}^{3\times3}$ is calculated as, $\mathbf{C} = \text{diag}(C_t, C_n, C_b)$, where C_t, C_n,

and C_b are the local resistance coefficients along the Frenet-Serret frames of the tail.[33] The two matrices presented in Equation (6) represent the resistance matrix of the tail, integral form, and the magnetic head of the swimmer. Due to linearity of Stokes flow of Equation (6), the resistance matrix of the swimmer, $\mathbf{M} \in \mathbb{R}^{6\times6}$, is calculated by superimposing the resistance matrices of its head and helical body, and we have

$$\mathbf{M} = \mathbf{M}_{\text{tail}} + \mathbf{M}_{\text{head}} \tag{7}$$

where $\mathbf{M}_{\text{tail}} \in \mathbb{R}^{6\times6}$ and $\mathbf{M}_{\text{head}} \in \mathbb{R}^{6\times6}$ are the resistance matrices of the helical tail and magnetic head, respectively.[34] Note that the these matrices contain the geometric parameters of the helical body (helix diameter, filament thickness, length, helicity angle, pitch) and the head. These parameters affect the swimming velocity through the relationship between $\boldsymbol{U}_r$ and $\boldsymbol{\omega}_r$, given by Equation (3) The RFT-based model can be adjusted to simulate the motion of helical microrobots while moving from one viscous fluid to another or through a Newtonian–viscoelastic interface. This concept is implemented by modifying the resistance matrix to account for the property of the two fluids separately. The integral operator in Equation (6), allows dividing the finite segments, ds, into two separate integrals using an intermediate point $\delta(s,t)$ which represents the position of the interface between the two fluids with respect to the counter length ℓ of the helical tail, such that

$$\begin{aligned}\mathbf{M}_{\text{tail}} = &\int_0^{\delta} \begin{bmatrix} \mathbf{R}\mathbf{C}_1\mathbf{R}^T & -\mathbf{R}\mathbf{C}_1\mathbf{R}^T\mathbf{S}_{\text{tail}} \\ \mathbf{S}_{\text{tail}}\mathbf{R}\mathbf{C}_1\mathbf{R}^T & -\mathbf{S}_{\text{tail}}\mathbf{R}\mathbf{C}_1\mathbf{R}^T\mathbf{S}_{\text{tail}} \end{bmatrix} \mathrm{d}s \\ &+ \int_{\delta}^{\ell} \begin{bmatrix} \mathbf{R}\mathbf{C}_2\mathbf{R}^T & -\mathbf{R}\mathbf{C}_2\mathbf{R}^T\mathbf{S}_{\text{tail}} \\ \mathbf{S}_{\text{tail}}\mathbf{R}\mathbf{C}_2\mathbf{R}^T & -\mathbf{S}_{\text{tail}}\mathbf{R}\mathbf{C}_2\mathbf{R}^T\mathbf{S}_{\text{tail}} \end{bmatrix} \mathrm{d}s \end{aligned} \tag{8}$$

where $\mathbf{C}_1$ and $\mathbf{C}_2$ are the viscous drag coefficient matrices of the low- and high-viscosity fluids, respectively. The resistance matrix $\mathbf{M}_{\text{tail}}$ can be redefined over each iteration based on the time-dependent value of penetration depth $\delta(s,t)$, as shown in Figure 1a. Note that the penetration depth $\delta(s,t)$ is defined for each arc length location s, $0 \le s \le \ell$. The resistance matrix $\mathbf{M}_{\text{head}}$ can be updated when the swimmer completely crosses the interface using the viscosity of the second fluids. Therefore, Equations (1) and (4)–(6) completes the hydrodynamic model of the magnetically driven helical microrobot inside a heterogeneous viscous fluid with space-varying viscosity. In the case helical propulsion between Newtonian and viscoelastic medium, the viscous torque can be replaced by the torque of the viscoelastic medium stiffness,[35] which depends on the elastic modulus E and the second integral in the right-hand side of Equation (8) has to be replaced with stiffness forces and torques.

Despite the linearity and time-independence of the viscous drag force and torque, nonlinearities resulting from the external magnetic actuation will govern the translational and rotational dynamics of the helical microrobot. This fact can be seen from Equations (1) and (2), by invoking the gradient of the magnetic field. The field falls off approximately as the inverse cube of the distance, whereas the gradient falls off as the inverse fourth power. Therefore, the dynamics of the helical robot is rewritten in a nonlinear state-space form, where the states ($\boldsymbol{x} \in \mathbb{R}^{6\times1}$) of the system are the 3D position of the CoM of the swimmer $\boldsymbol{r} = \{x, y, z\}$ and the three angles (α, β, γ) which represent its orientation with respect to the global frame of reference in terms of rotations around the x-, y-, and z-axis, respectively (Figure 1a). They are the integral of the angular velocities $\boldsymbol{\omega}_r$ and used to define the rotation matrix from the local swimmer frame to the global frame of reference as follows

$$\mathbf{R}_{\text{Lab}} = \mathbf{R}_z(\gamma)\mathbf{R}_y(\beta)\mathbf{R}_x(\alpha) \tag{9}$$

where $\mathbf{R}_x(\alpha) \in \mathbb{R}^{3\times3}$ is a rotation matrix describing a rotation of an angle α about the x-axis. The modeled actuation strategy is ideal radial control. The relation depends on parameters (λ) such as distance from the magnet ($\boldsymbol{p}$) and actuation frequency (f). The state-space model is given by

$$\dot{\boldsymbol{x}} = \boldsymbol{g}(\boldsymbol{x}, \lambda, t), \qquad \boldsymbol{x}(t_0) = \boldsymbol{x}_0 \tag{10}$$

where $\boldsymbol{g} : \mathbb{R}^{n\times1} \to \mathbb{R}^{n\times1}$, $\boldsymbol{x} \in \mathbb{R}^{n\times1}$ is the state vector of the system, $\lambda \in \mathbb{R}^{k\times1}$ is the vector of parameters, and $\boldsymbol{x}_0 \in \mathbb{R}^{n\times1}$ is a vector of the initial position and orientation of the helical microrobot.

2.3. Numerical Solutions of Helical Propulsion between Viscous Fluids

Numerical solutions for the magneto-hydrodynamic model described by Equations (1)–(10) are found in order to study the influence of the magnetic, geometric, and rheological parameters on the overall behavior of the helical microrobot. **Figure 2**a shows the 3D trajectory of a helical robot, actuated at frequency of f = 5 Hz, swimming from low- to high-viscosity fluids (η_1 = 5 Pa s and $\eta_2 = 2\eta_1$ Pa.s). The simulations are performed using ideal radial control[19] prescribing a linear motion along the x-axis, which means that the RPM is aligned with the magnetic head of the untethered helical robot in the x–y plane and at a constant distance along the z-axis. We consider three distinct parameters (f, p, and η_0) to predict the response of the helical robot. The actuation frequency is varied for a range between 2 and 10 Hz, and the distance between the RPM and the helical robot is varied between 7.5 to 8.5 body lengths of the helical robot. The viscosity ratio is varied for a range between 1.3 to 2.3. The actuation frequency range is chosen based on the minimum propulsive thrust that can lead to propulsion and the step-out frequency which limit the minimum and maximum actuation frequencies, respectively. The relative distance $\|\boldsymbol{p}\|$ is selected such that the magnitude of the rotating magnetic field is limited for a range between 1.5 and 2.5 mT. Finally, the ratio η_0 is selected based on the dependence of the human blood viscosity on temperature for a fixed shear rate. The viscosity of blood plasma decreases by 10% for a 5 °C increase in the temperature.[36]

Figure 2a shows the trajectory taken by the helical robot between two fluids at actuation frequency of 5 Hz. At η_1 = 5 Pa s, the average swimming speed is 5.02 mm s^{-1} and it decreases to 3.16 mm s^{-1} after crossing the interface of the second fluid (η_2 = 10 Pa s). The evolution of the CoM in the y–z plane (Figure 2b) shows wobbling and drifting while swimming forward along the x-axis of the global reference frame. Once the tip of the

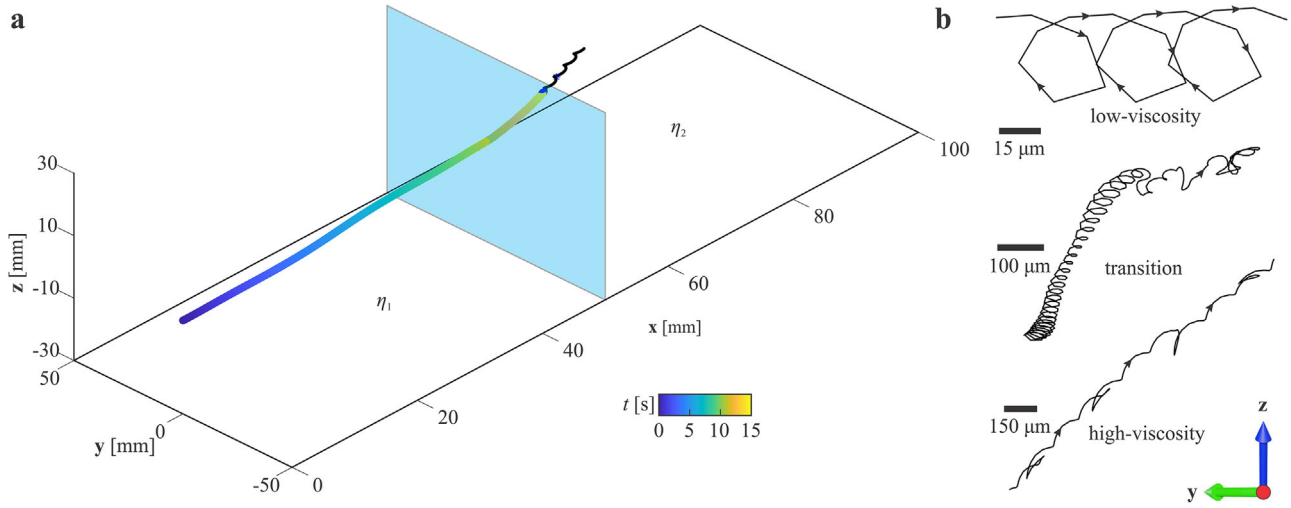

Figure 2. Trajectory of the center of mass (CoM) of the helical robot is calculated during motion between two fluids with viscosity of $\eta_1 = 5$ Pa s and $\eta_2 = 10$ Pa s, under the influence of a time-periodic rotating magnetic field ($f = 5$ Hz). a) At the low-viscosity fluid, $U_r = 5.02$ mm s^{-1}. At the high-viscosity fluid, $U_r = 3.16$ mm s^{-1}. The transparent plane represents the interface between the low- and high-viscosity fluids. b) The evolution of the CoM in the y–z plane shows that the amplitude of the periodic solution decreases as the helical body transitions through the interface. The periodic solution with smaller amplitude is observed after completely crossing the interface between the two fluids.

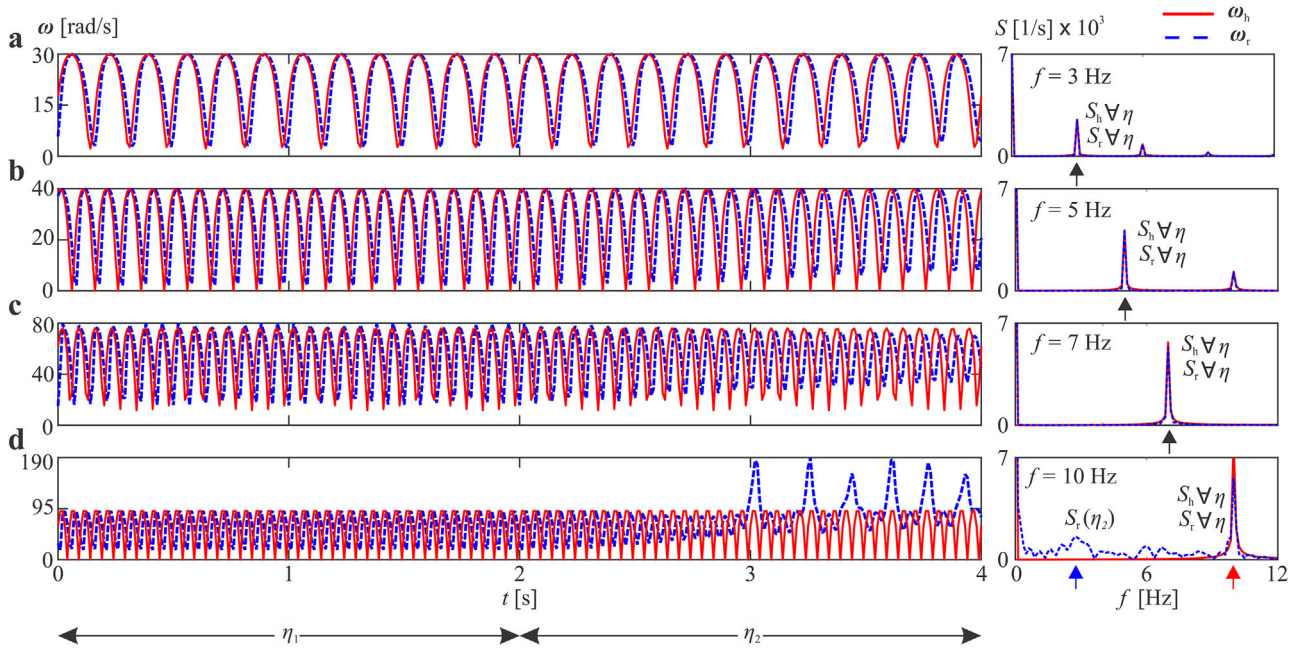

Figure 3. The angular velocities of the robot, ω_r, and the actuating field ω_h, and their corresponding power spectra reveal the influence the viscosity ratio, $\eta_0 = \eta_2/\eta_1$, and actuation frequency, f, on the ability of the helical robot to rotate in sync. The angular velocity of the helical robot ω_r, with respect to the x-axis, is plotted with the field rotational speed ω_h when the swimmer reaches the interface between two fluids with viscosity $\eta_1 = 5$ Pa s and $\eta_2 = 1.8\eta_1$ at $t = 2$ s. a) At $f = 3$ Hz, the power spectra of the helical robot and the field, S_r and S_h, are identical regardless of the viscosity. b) At $f = 5$ Hz, the power spectrum S_r is less than S_h by 0.5%. c) At $f = 7$ Hz, the power spectrum S_r is less than S_h by 6.2%. d) At $f = 10$ Hz, the power spectrum S_r is less than S_h by 32.0% for η_1, and when the robot transitions to the high-viscosity fluid the power spectrum at 2.7 Hz is decreased by 80.5%.

helical body comes into contact with the interface between the two fluids ($\delta = 0$), the amplitude of the periodic wobbling of the CoM decreases and the motion becomes irregular until the helical body transitions into the high-viscosity fluid ($\delta > L$). In this case, the amplitude of the wobbling CoM is decreased with the swimming speed while drifting along the y-axis.

A simple approach to understanding how transitioning between two fluids affects the trajectory is to predict the response at actuation frequency range of $2 \leq f \leq 10$ Hz. **Figure 3** shows the angular velocities of the microrobot and the actuating field for all the frequencies and for ratio between the viscosity of the mediums $\eta_0 = 1.8$. At $f = 3$ Hz, the abrupt change in rheologi-

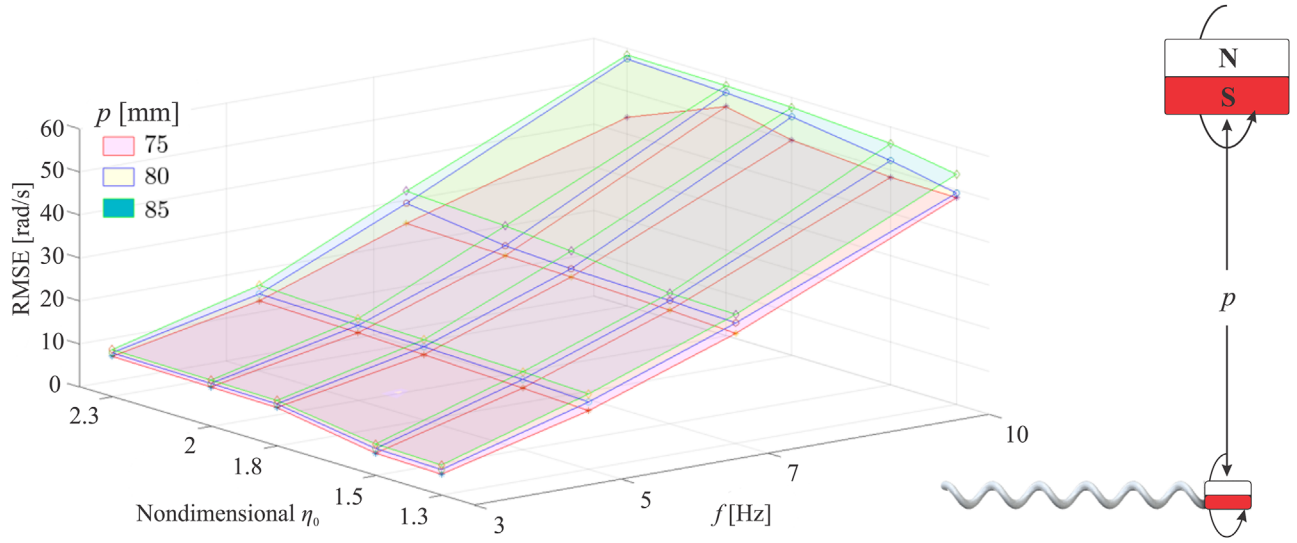

Figure 4. The root-mean-square error (RMSE) between the simulated angular velocities of the swimmer $\boldsymbol{\omega}_r$ and field $\boldsymbol{\omega}_h$ are calculated for each combination of actuation frequencies (f = [3, 5, 7, 10] Hz), relative position of the RPM ($\boldsymbol{p}$ = [75, 80, 85] mm) and viscosity ratios between the two fluids $\eta_0 = \eta_2/\eta_1$ = [1.3, 1.5, 1.8, 2, 2.4]. The RMSE increases with $\boldsymbol{p}$ and η_0 since higher values of these parameters reduce ω_{so} and the response of the helical robot to higher f results in $\omega_r > \omega_{so}$.

cal properties does not seem to affect the ability of the swimmer to rotate in sync with the field, as shown in Figure 3a, using the power spectra (right panel) corresponding to the time series of the angular velocities (left panel). In this case, the helical microrobot rotates with the same frequency of the field as reflected by the corresponding power spectra S_r and S_h of the microrobot and the field, respectively, for all fluid viscosities. The power spectrum S_r is identical to the power spectrum S_h for the two viscosities. As the actuation frequency increases to $f = 5$ Hz, the difference between S_r and S_h increases to 0.5%, as shown in Figure 3b. Note that as the actuation frequency of the magnetic field increases the frequency of the helical robot must also increase in order to increase the propulsive thrust based on Equation (6). The power spectra in Figure 3a,b indicate that motion enhancement is possible below actuation frequency of 5 Hz because of the magneto-hydrodynamic synchronization. At $f = 7$ Hz (Figure 3c), a reduction of 6.2% is calculated between the power spectra of the robot and the magnetic fields as reflected by the Fourier peaks at 7 Hz for the low- and high-viscosity fluids. At $f = 10$ Hz, we observe a reduction of 80.5% at the low-viscosity fluids as reflected by the Fourier peaks at 10 Hz in Figure 3d, whereas the Fourier peak at frequency 2.7 Hz (small blue arrow) is associated with the angular velocity of the helical robot in the high-viscosity fluid. At this actuation frequency, the helical microrobot cannot rotate in sync with the field and thus reaching step-out frequency ω_{so}. The step-out frequency is proportional to the applied magnetic torque by a viscous drag coefficient c, which varies with surface friction, fluid viscosity, and microrobot geometry,[37] as follows

$$\|\boldsymbol{\omega}_{so}\| = \frac{1}{c}\|\boldsymbol{m}_r\|\|\boldsymbol{B}(\boldsymbol{p})\| \tag{11}$$

To compare the results of the simulations, the root-mean-square error (RMSE) between the magnetic field angular velocity ω_h and swimmer ω_r, with respect to the x-axis, is calculated using

$$\text{RMSE} = \sqrt{\frac{\sum_{n=1}^{N}(\omega_h - \omega_r)^2}{N}} \tag{12}$$

where N is the number of samples of the calculated angular frequencies. The error increases with the viscosity ratio (η_2/η_1), actuation frequency (f), and actuation distance ($\|\boldsymbol{p}\|$) as expected from Equation (11). Increasing the distance $\|\boldsymbol{p}\|$ decreases the magnetic field and the corresponding magnetic torque, while c increases with the viscosity. For $f = 5$ Hz, the errors are already substantial (≈20 rad s^{-1}) suggesting that the helical robot is not rotating in sync with the field, as shown in **Figure 4**.

3. Sensitivity Analysis of the RFT-Based Model

Sensitivity analysis can identify key parameters whose uncertainty affects the outputs. It reveals priorities of each parameter, in terms of their influence on the states, thereby making the precise identification and control of some parameters more critical and establish priorities during design and experimental work. Using the state Equation (10), we have[38]

$$\mathbf{S}(t) = \frac{\partial \boldsymbol{x}}{\partial \boldsymbol{\lambda}}(t, \lambda) \tag{13}$$

where $\mathbf{S}(t) \in \mathbb{R}^{n\times k}$ is the sensitivity function. To define Equation (13), the integral form in time domain of Equation (10) gives relevant information about the initial conditions of the sensitivity function $\mathbf{S}(t_0)$. The integral form in the time domain is given by

$$\boldsymbol{x}(t) = \boldsymbol{x}_0 + \int_{t_0}^{t} \boldsymbol{g}\big(s, \boldsymbol{x}(s, \lambda), \lambda\big)\mathrm{d}s \tag{14}$$

Differentiation with respect to λ yields

$$\frac{\partial \boldsymbol{x}}{\partial \lambda}(t,\lambda) = \int_{t_0}^{t} \frac{\partial \boldsymbol{g}}{\partial \boldsymbol{x}}(s,\boldsymbol{x}(s,\lambda),\lambda) + \frac{\partial \boldsymbol{g}}{\partial \lambda}(s,\boldsymbol{x}(s,\lambda),\lambda)\mathrm{d}s,$$
$$\mathbf{S}(t_0) = \frac{\partial \boldsymbol{x}}{\partial \lambda}(t_0,\lambda) = \frac{\partial \boldsymbol{x}_0}{\partial \lambda} = 0 \tag{15}$$

Equation (15) defines the initial values of the sensitivity function at $t = t_0$ to be zero since $\boldsymbol{x}_0$ is independent of λ. To determine the evolution of the sensitivity function, matrices of partial derivatives presented in Equation (15) are defined as follows

$$\mathbf{A}(t,\lambda) = \frac{\partial \boldsymbol{g}}{\partial \boldsymbol{x}}(t,\boldsymbol{x}(t,\lambda),\lambda)\Big|_{x=x(t,\lambda)},$$
$$\mathbf{B}(t,\lambda) = \frac{\partial \boldsymbol{g}}{\partial \lambda}(t,\boldsymbol{x}(t,\lambda),\lambda)\Big|_{x=x(t,\lambda)} \tag{16}$$

where $\mathbf{A} \in \mathbb{R}^{n\times n}$ and $\mathbf{B} \in \mathbb{R}^{n\times k}$ are the matrices of partial derivatives of the function $\boldsymbol{g}$ calculated with respect to the state variables $\boldsymbol{x}$ and the parameters λ, respectively. Differentiating Equation (15) with respect to time, we obtain

$$\frac{\partial}{\partial t}\frac{\partial \boldsymbol{x}}{\partial \lambda}(t,\lambda) = \mathbf{A}(t,\lambda)\frac{\partial \boldsymbol{x}}{\partial \lambda}(t,\lambda) + \mathbf{B}(t,\lambda) \tag{17}$$

The sensitivity function $\mathbf{S}(t)$ is the unique solution of Equation (17), then substituting Equation (13) into Equation (17), we have

$$\dot{\mathbf{S}}(t) = \mathbf{A}(t,\lambda)\mathbf{S}(t) + \mathbf{B}(t,\lambda) \tag{18}$$

The sensitivity functions provides first-order estimates of the effect of parameter variations on the state variables of the system using the sensitivity Equation (18). The elements of the sensitivity function $\mathbf{S}_{ij}(t)$ are used to create an augmented state-space system and its dynamic evolution is studied with the initial states by integrating Equation (18). The sensitivity functions are defined based on the state variables and the input parameters such that the indices i and j indicate the ith state variable and jth input parameter. These new states show the effect of uncertainty in the parameters on the original states. For example, if the sensitivity function S_{ij} has a constant value of zero then the state variable x_i is not sensitive to variations in the input parameter λ_j, and If the sensitivity function S_{ij} varies with time then it is sensitive to uncertainty in the input parameter λ_j. Note also that for multiple nonzero time-varying sensitivity functions, we can identify states that are affected by an input parameter more than other states.

3.1. Numerical Solutions of the Sensitivity Analysis

After defining the sensitivity function of the RFT-based model, nominal values are given to the parameters and the evolution of the augmented system over time is estimated. The analysis is implemented using a nominal viscosity of $\eta = 5$ Pa s and the nominal values given to the parameters are $f = 3$ Hz and $p = 7.5$ cm. Note that the helical robot is rigid and its geometric parameters have constant values, and its magnetic moment is effectively constant with respect to the body regardless of the applied field. Therefore, the geometric and magnetic parameters of the helical robot are fixed. The results of the sensitivity equation can be nondimensionalized and normalized in order to compare the effect of each input parameter on a state variable. For example, $S_{21} = \gamma_f$ and $S_{22} = \gamma_p$ are the new sensitivity functions describing the effect of $\lambda_1 = f$ and $\lambda_2 = p$, respectively, on the state variable γ (transverse displacement). To compare them, all augmented states and sensitivity functions are normalized using their maximum value over time, thereby nondimensionalized for a range between 0 and 1. Therefore, the nondimensionalized and normalized sensitivity functions, $\hat{\mathbf{S}}(t)$, are calculated using

$$\hat{\mathbf{S}}(t) = \frac{\mathbf{S}(t)}{\max(\mathbf{S})} \tag{19}$$

where $\max(\mathbf{S})$ is the maximum of the function $\mathbf{S}$. **Figure 5** shows the results of the augmented state model which includes six state variables and twelve sensitivity functions corresponding to two input parameters.

Figure 5a shows the wobbling and drifting response of the CoM of the helical robot. The wobbling and drifting (in the x–y plane) is accompanied with an increase of the state variable x with time. The angular rotations about the y-axis, β, and z-axis, γ, show a small-amplitude periodic orbit in time, as shown in Figure 5b. Similarly, Figure 5c shows a small-amplitude periodic orbit for the angular rotations about the x-axis, α, and z-axis, γ. The transverse velocities of the helical robot, U_y and U_z, demonstrate periodic limit cycle motion that depends on the frequency of the actuating magnetic field, as shown in Figure 5d. The transnational speed, U_x, and the angular velocities $\dot{\gamma}$ and $\dot{\beta}$ also converge to their respective limit cycles as the robot swims under the influence of the periodic input torque of the rotating magnetic field, as shown in Figure 5e,f, respectively.

The sensitivity functions of the helical robot are shown in Figure 5g–l. The sensitivity function $S_{11} = x_f$ of the first state variable (position along the x-axis) with respect to the actuation frequency $\lambda_1 = f$ is shown in Figure 5g. S_{11} has a time-periodic pattern with an increasing envelop signifying the sensitivity of the state variable x to the actuation frequency. Likewise, $S_{12} = x_p$ is time-periodic with small-amplitude and an increasing envelop. Therefore, this state variable is also sensitive to the relative distance, p, between the helical robot and the actuator magnet. However, it is more sensitive to variation in actuation frequency than to variation in the relative distance p. The second state variable y of the helical robot is as sensitive to the actuation frequency as the first state variable x, as shown in Figure 5h, where $S_{21} = y_f$ oscillates increasingly with time. Similarly, the sensitivity function $S_{22} = y_p$ indicates the transverse displacement of the helical robot is less sensitive to the relative distance than the actuation frequency. The transverse displacement along the z-axis has sensitivity functions similar to the transverse displacement along the y-axis, as shown in Figure 5i. Again, $S_{31} = z_f$ and $S_{32} = z_p$ indicate that the transverse displacement z is more sensitive to actuation frequency than the relative distance p.

Unlike the transnational states of the helical robot, the sensitivity functions corresponding to angular orientations have unique

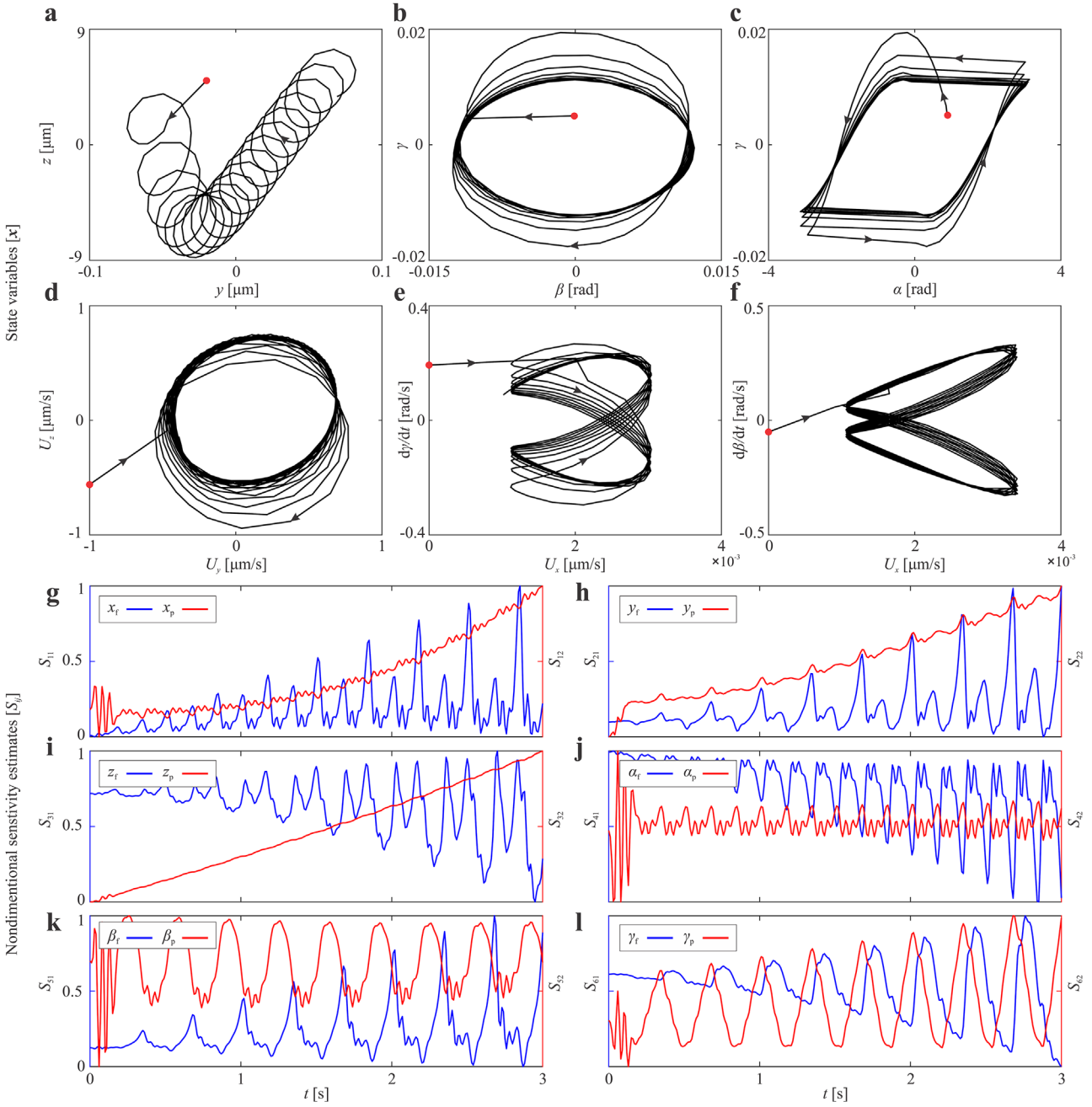

Figure 5. Solutions of the nonlinear state Equation (10) and the time-varying sensitivity Equation (18) highlight the influence of input parameters. The nominal value given to the parameters are $p = 7.5$ cm, $f = 3$ Hz, and $\eta = 5$ Pa s. a–f) State variables show time-periodic behavior. The small red circle indicates the initial state. g–l) Nondimensionalized and normalized sensitivity functions vary in time, showing the sensitivity of the *i*th state to the *j*th input parameter.

patterns. Figure 5j shows that the sensitivity function, $S_{41} = \alpha_f$, of the angular orientation with respect to the x-axis oscillates increasingly with time, while $S_{42} = \alpha_p$ periodically vary in time with small-amplitude. Therefore, the state variable α is more sensitive to variations in actuation frequency f than to variations in the relative distance p. Note that the state variable α describes the rolling motion of the helical robot about its long axis. Such motion is highly sensitive to the actuation frequency and is less influenced by the relative distance p. If the relative distance p is high enough for the magnetic field to become uniform at the position of the helical robot, then the robot will be affected by torques about the y- and z-axis, resulting in yawing and pitching motion, respectively. The influence of the input parameters f and p on the yawing motion and pitching motion is shown in Figure 5k,l, respectively. The sensitivity functions $S_{51} = \beta_f$ of the yawing motion and $S_{61} = \gamma_f$ of the pitching motion to the actua-

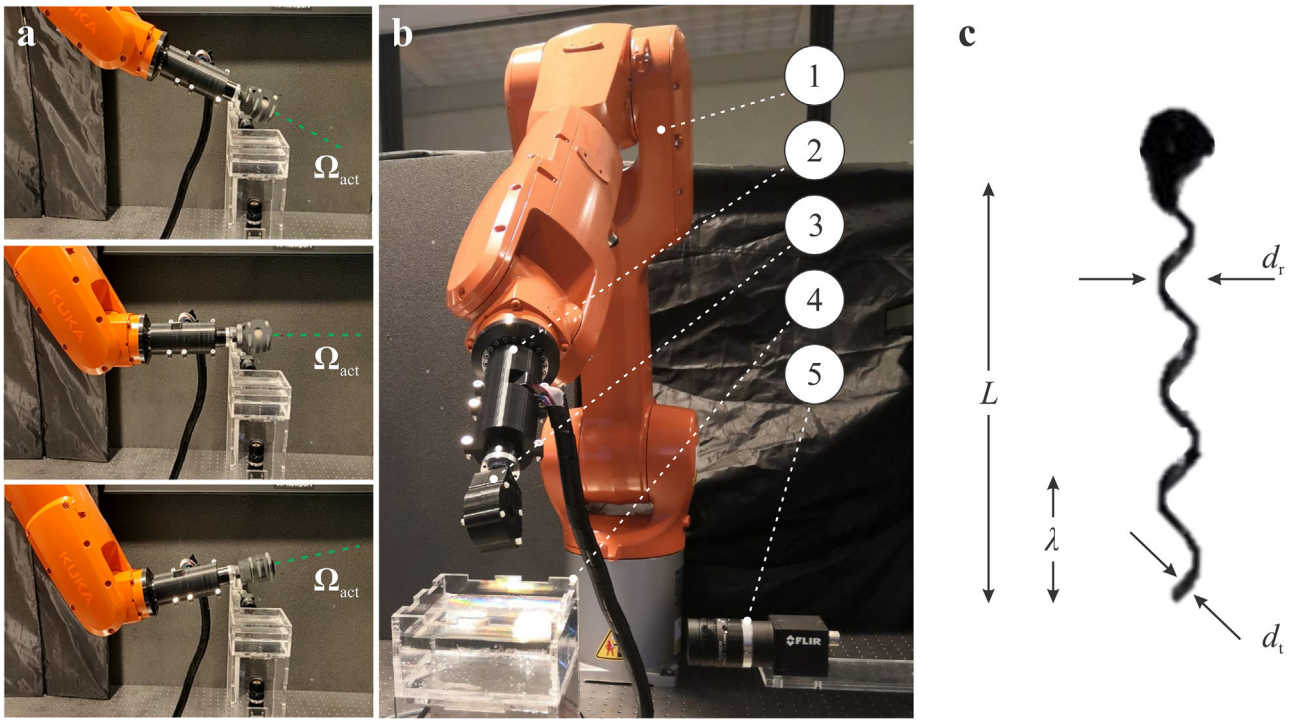

Figure 6. Helical propulsion is achieved using rotating dipole fields generated by a permanent-magnet robotic system. a) The rotation axis of the permanent magnet is controlled to steer the helical robot in 3D space. b) A robotic manipulator ① (KUKA KR-1100-2) controls the pose of a DC motor ② and a permanent magnet ③. The helical robot is contained inside a viscous fluid container ④ and its motion is tracked using two cameras ⑤. c) The robot consists of a helical body with length L and diameter d_r attached to a small permanent magnet with magnetization perpendicular to its long axis.

tion frequency are quite similar. Both functions oscillate increasingly in time, indicating that the state variables β and γ are sensitive to variations in the actuation frequency. However, yawing motion and pitching motion are more sensitive to the relative distance p than to variations in the actuation frequency f. Note also that the geometric and magnetic parameters of the helical robot have constant values due to the rigidity of the structure and the permanently magnetized head. In the case of a soft-body and a soft-magnetized head, the body will deflect due to the viscous drag encountered and the magnetization will vary as a nonlinear function of the applied field; the sensitivity functions would be significantly more complex.

4. Motion Control Experimental Results

A permanent-magnet robotic system is used to experimentally test the sensitivity of the helical robot to input parameters. The actuation frequency and the relative distance between the actuator magnetic and the helical robot are critical parameters in wireless manipulation using external magnetic fields.

4.1. Permanent-Magnet Robotic System

The permanent-magnet robotic system consists of a 6-DOF serial manipulator (KUKA KR-1100-2, KUKA, Augsburg, Germany) to control the displacement of the RPM (**Figure 6**).[39] The permanent magnet is an axially magnetized disk (NdFeB Grade-N45) with a diameter of 35 mm and a height of 20 mm and its magnetization has been experimentally measured to be $\|\boldsymbol{M}_{act}\| = 18.89$ A m^2. A Maxon 18 V brushless DC motor with Hall-effect sensors, encoder, and a planetary gearbox with a gear ratio of 3.7:1, is used to actuate the permanent magnet. The motor is controlled using an EPOS4 Compact 50/5 CAN, digital position controller. The continuous rotation of the permanent magnet enables the robot to achieve helical propulsion. The helical robot consists of a cylindrical permanent magnet (NdFeB Grade-N52) with 1 mm diameter and 1 mm height, attached to a helical body such that the helix axis is perpendicular to the dipole moment. The helix has length L, pitch λ, and radius $d_r/2$ of 11.7 mm, 3 mm, and 0.6 mm, respectively, see **Table 1**. The size of the helical robot is in the millimeter range and low-Re on the order of 10^{-4} is approached through the use of high-viscosity fluids. Therefore, the experimental results qualitatively captures the characteristics of the flow when the helical robot is downscaled to submillimeter range and microscale. The geometric parameters

Table 1. Geometric and magnetic parameters of the helical robot used in experiments and numerical analysis. The geometric parameter of the rigid helix are the length L, pitch λ, diameter d_r, and filament thickness d_t.

	Property	Value	Property	Value
Helical body	L [mm]	11.7	λ [mm]	3
	d_r [mm]	1.2	d_t [mm]	0.12
Magnetic head	Type	disk NdFeB	d [mm]	1
	m_r [A m^2]	6.23×10^{-4}	h [mm]	1

of the helical body and the head provides maximum swimming velocity based on the relationship between the transnational and rotational velocities in Equation (6).

The motion of the helical robot is recorded by two FLIR Blackfly cameras (Teledyne FLIR LLC, Willsonville, Oregon) in the x–y and y–z planes. Both of these cameras are fitted with a Fujinon lens of 6 mm fixed focal length producing submillimeter tracking accuracy at 60 frames per second. The entire system is programmed and modeled using Matlab (The MathWorks, Inc., Natick, MA, USA) and custom-made Matlab routines. To implement real-time control of the robotic manipulator, a connection between RoboDK (RoboDK Inc., Montreal, Canada) and the robotic manipulator is established to move it automatically using RoboDK's user interface. The connection was realized through a standard Ethernet connection (TCP/IP). For this purpose, a KUKAVARPROXY (Imts Srl, Taranto, Italy) server is installed on the KRC4 controller (KUKA, Augsburg, Germany) of the robotic manipulator. This server allows the global variables from the robotic arm controller to be exchanged with the remote RoboDK's user interface. The workspace consists of a plexiglass box ($100 \times 100 \times 50$ mm^3) filled in equal volume with silicone oil ($\rho_f = 971$ kg m^{-3} and $\eta = 5$ Pa s) and tissue-mimicking gelatin phantom.[40] The dry-weight concentration ratio of the gelatin and water is 2%, resulting in a minimum and maximum viscosity of 0.77 ± 0.1 and 4.39 ± 0.01 Pa.s for a frequency range (strain rate) between 2 and 25 Hz, respectively. The maximum elastic modulus of the medium was measured to be $E = 688$ Pa. The mechanical properties of the phantoms were stable after the addition of the silicone oil throughout the period of each motion control trial. In each trial, the helical robot performs a motion of ≈70 mm along the x-axis, crossing the interface positioned at ≈48 mm. The transverse displacement along the y-axis is similar with a value of ≈20 mm. At $f = 3$ Hz, the initial distance from the permanent magnet is $\boldsymbol{p} = 7.5$ cm and the helical robot reaches the interface at 12 mm with respect to the z-axis, while for $f = 2$ Hz, $\boldsymbol{p} = 8.2$ cm and it crosses the interface at a height of 7 mm.

4.2. Motion between Newtonian and Viscoelastic Mediums

To test the sensitivity of the helical robot to variations in actuation frequency and variations in the rheological properties of the medium, propulsion is achieved between silicone oil and gelatin using a single RPM. Linear motion along the x-axis is prescribed to the end-effector while keeping the rotation axis $\hat{\boldsymbol{\Omega}}_{act}$ in a parallel configuration with the x-axis, resulting in the same unidirectional motion of the helical robot by aligning with the rotating magnetic field in synchrony about $\hat{\boldsymbol{\omega}}_h \parallel \hat{\boldsymbol{\Omega}}_{act}$. The linear velocity of the end-effector is adjusted experimentally for each actuation frequency to perform radial control of the helical robots.

Figure 7a shows the position of the helical robot over time during a representative open-loop motion control experiment at actuation frequency of $f = 2$ Hz (66% of the limiting step-out frequency), and the velocity is calculated by postprocessing the recorded motion. The helical robot is radially actuated and reaches maximum swimming speed of 2.5 mm s^{-1} at $t = 7$ s ($Re = 10^{-4}$). The robot follows a path with nonzero curvature as a consequence of the asymmetric transverse viscous drag forces and torques, Equation (6), along the helical body, as shown in Figure 7b. Note that the curvature of the trajectory of the helical robot in the silicone oil is greater than that in the gelatin. Associated with the transitioning between the two environments is a change in the ratio of magnetic torque to viscous drag, $\|\boldsymbol{m}_r\|\|\boldsymbol{B}\|/\|\boldsymbol{\tau}_{visc}\|$, and magnetic torque to gelatin stiffness, $\|\boldsymbol{m}_r\|\|\boldsymbol{B}\|/d_r^3 E$. This transition leads to different curvatures between the taken pathways for the same actuation parameters. Before the silicon–gelatin interface, the curvature of the trajectory is relatively high and it decreases significantly when the robot transitions in the gelatin. The difference in curvature is attributed to two key reasons. First, the torque balance in silicone oil differs from that in gelatin in that the first is between the magnetic and viscous drag, whereas the second is between the magnetic and the stiffness of the viscoelastic medium. Second, the force balance in the two environments affects the transnational velocity and their frequency response. Figure 7c shows the instantaneous swimming velocities of the helical robot throughout the nonzero curvature path. The speed decreases significantly as the robot approaches and crosses the interface. The average swimming speed decreases from 2.5 mm s^{-1} in silicone oil to 0.5 mm s^{-1} in gelatin. Nevertheless, the robot maintained its forward swimming direction under the open-loop action of the rotating magnetic field.

Sensitivity analysis suggests that the state variables of the helical robot are more sensitive to variation in actuation frequency than to variation in the relative distance between the robot and the actuator magnet, as shown in Figure 5g–l. Therefore, we increase the frequency of the rotating magnetic field to 100% of the limiting step-out frequency and repeat the open-loop actuation, in a manner similar to the experiment before. **Figure 8** shows the position of the helical robot over time under the influence of a rotating magnetic field with frequency of $f = 3$ Hz. The robot is radially actuated in an open-loop fashion and reaches maximum speed of 2.71 mm s^{-1} at $t = 7$ s ($Re = 10^{-4}$). At $t = 10$ s, the helical robot is propelled while it is not aligned with $\hat{\boldsymbol{\omega}}_h \parallel x$-axis and the angle between this axis and the long axis of the helix remains constant after crossing the interface. The magnetic head reaches the interface at $t = 20$ s, and swims along a path with relatively small nonzero curvature in the direction of the orientation of the helix axis from $t = 30$ s when the helical body is completely immersed in the gelatin phantom. Minimum speed of 0.2 mm s^{-1} is measured at $t = 34$ s, while the robot is drilling inside the stiffer portion of the gelatin phantom which is not in contact with the silicone oil. At this time, the forward speed increases and the helical robot becomes able to swim in the viscoelastic medium. The maximum speed in the gelatin phantom is 1.44 mm s^{-1} (at $t = 77$ s).

Open-loop motion control results show that the robot remains within a smaller domain in the y–z plane as it swims forward along the x-axis when actuated at 66% of its step-out frequency. In this case the robot wobbles and shifts within a rectangular region with edge length of $\Delta y = 22.1$ mm and $\Delta z = 7.2$ mm along the y-axis and z-axis, respectively, as shown in Figure 7b. This area increases to $\Delta y = 19.2$ mm and $\Delta z = 11$ mm along the y-axis and z-axis, as shown in Figure 8b, respectively, when the robot is actuated at its step-out frequency. The area in which the robot wobbles and drifts while swimming forward increased by 32% when the actuation frequency is increased by 1 Hz. All sensitivity functions of the helical robot to variation in the actuation frequency indicate that the state variables are affected by the actuation fre-

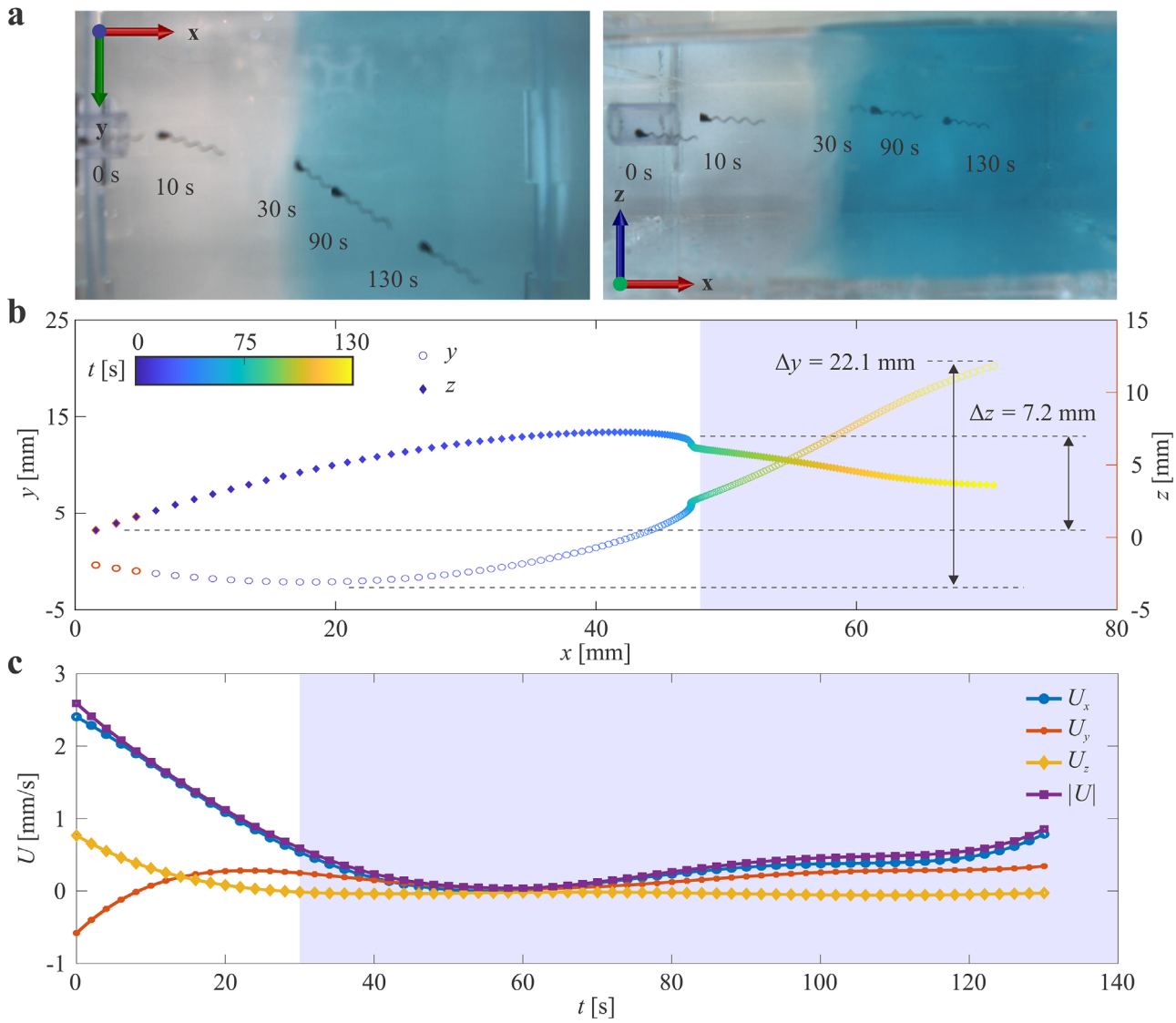

Figure 7. Low-actuation frequency at 2 Hz enables helical propulsion between a Netwonian fluid and viscoelastic medium using rotating magnetic fields. a) Top- and side-views (x–y plane and x–z plane) of the swimming path of the helical robot. The robot transitions from silicone oil to tissue-mimicking gelatin phantom. b) Despite the difference in rheological properties, the measured 3D trajectory of the robot shows its capability to maintain its swimming direction. The magnetic head reaches the interface between the two mediums at $t = 30$ s (in blue). c) The swimming speed decreases near the interface between the two mediums, starting at 2.5 mm s^{-1} and reaching 0.5 mm s^{-1} in the Newtonian and viscoelastic fluids, respectively ($Re \approx 10^{-4}$).

quency. Although it is straightforward to understand and relate the actuation frequency to the instantaneous swimming velocities based on the relationship between the viscous drag force and velocities using Equation (6), our sensitivity analysis captures additional physical aspect of the actuation using rotating magnetic fields. The sensitivity functions S_{51} and S_{61} (Figure 5k,l) reveals that the yawing motion and pitching motion are sensitive to the actuation frequency. Therefore, a slight increase in the actuation frequency can affect not only the swimming velocity of the helical robot, but also the nonzero curvature of the swimming path.

Finally, it is possible to use the results of the sensitivity analysis to identify key control variables and geometric features, and then apply open-loop control in situations where we cannot introduce feedback. This approach has the potential for improved wireless actuation response, even with open-loop control system.

5. Discussions

Magnetically-actuated helical robots are promising as untethered devices for medical applications since they can perform 3D navigation under the influence of low-strength rotating magnetic fields.[41,42] Their motion at low-Re is simulated using an RFT-based model, allowing us to calculate instantaneous velocities and displacements in 3D space. This model is used to characterize the motion of helical robots while swimming from low to high viscosity. The simulations show how abrupt changes in rhe-

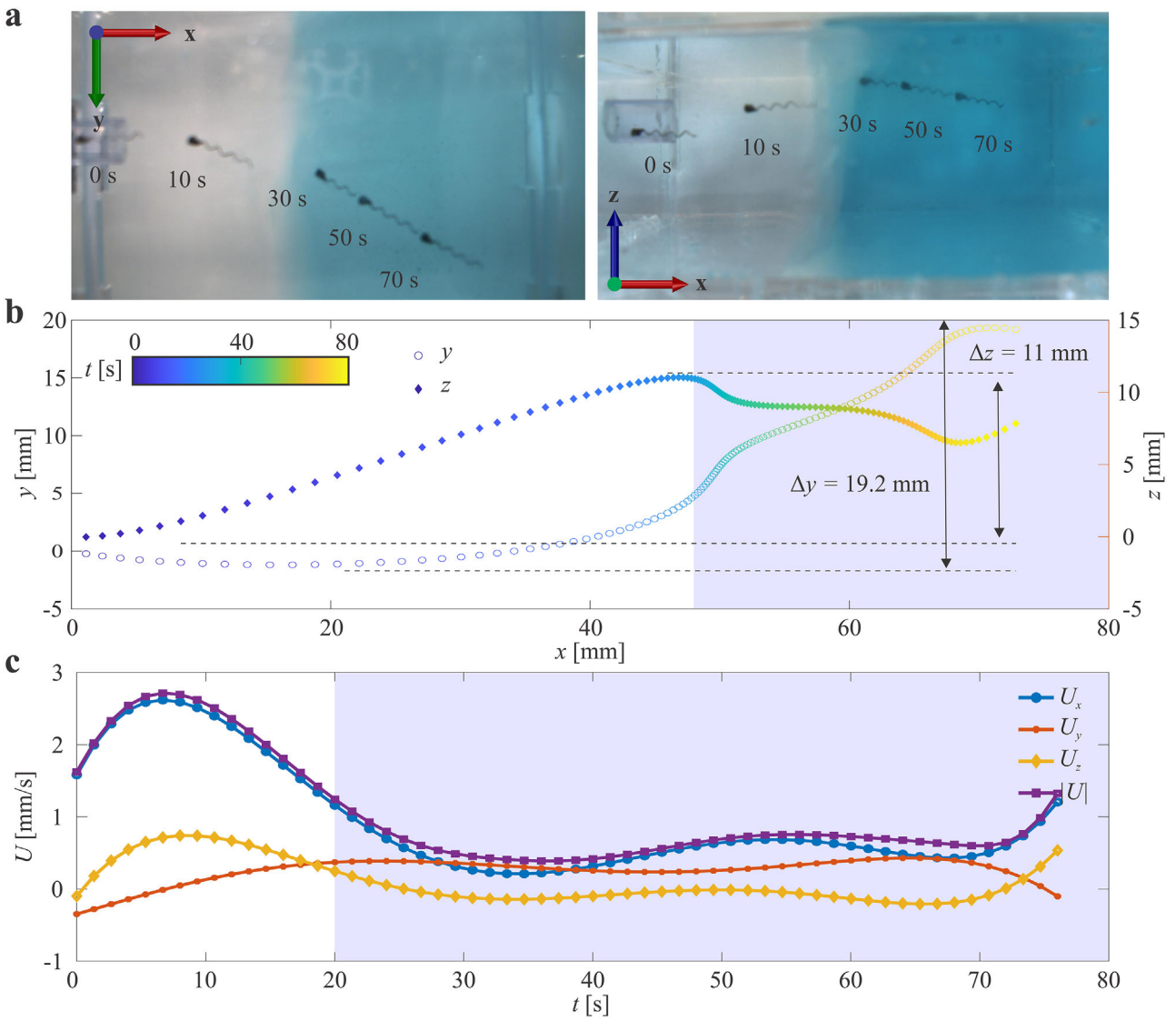

Figure 8. Low-actuation frequency of 3 Hz enables helical propulsion between Netwonian fluid and viscoelastic medium using rotating magnetic fields. a) Top- and side-views (*x*–*y* plane and *x*–*z* plane) of the swimming path of the helical robot. The robot transitionsfrom silicone oil to tissue-mimicking gelatin phantom. b) Despite the difference in rheological properties, the measured 3D trajectory of the robot shows its capability to maintain its swimming direction. The magnetic head reaches the interface between the two mediums at $t = 20$ s (in blue). c) The swimming speed decreases near the interface between the two mediums, reaching maximum speed of 2.7 mm s^{-1} and decreasing to 0.75 mm s^{-1} in the Newtonian and viscoelastic fluids, respectively ($Re \approx 10^{-4}$).

ological properties can affect the motion when the helical robot rotates close to step-out frequency. Furthermore, the proposed sensitivity analysis shows the impact of the input parameters $\boldsymbol{p}$ and f on the overall motion. The states of the system are more sensitive to variations in frequency than in actuation distance. In fact, when the helical robot rotates at $\omega_r < \omega_{so}$, variations in $\boldsymbol{p}$ do not have a strong impact on the states as long as the applied field is strong enough to set $\omega_{so} > \omega_r$. With these experiments, we demonstrate the ability of helical robots to propel both in Newtonian fluid and viscoelastic medium while being actuated using a single RPM attached to a serial manipulator in an open-loop fashion. The presented setup can actuate helical robots both in Newtonian and viscoelastic mediums. The presented model and the sensitivity analysis have shown which parameters must be controlled owing to its influence on the state variable. The two analyses converged to a common solution to controllably actuate helical robots. Decreasing the actuation frequency and increasing magnetic field strength, if applicable, can decrease the sensitivity of the helical robot to physical surroundings. In fact, the robot must rotate below ω_{so} which changes based on the rheological properties and the applied field.

Straight runs of the helical robot in the non-Newtonian or viscoelastic mediums (bodily fluids and soft-tissue environment) cannot be achieved without feedback control and noninvasive imaging systems. The localization and tracking is very difficult for some noninvasive imaging methods in challenging environ-

ment inside the human body such as regions with air-pockets, bony structures, and other wave reflectors.[43,44] The localization is more difficult for the majority of noninvasive imaging systems when the robot's size is decreased. In this case, the contrast-to-noise ratio decreases and impairs accurate and stable localization. Therefore, feedback control systems are likely to be affected by the increased sensory uncertainty during in vivo trials. The RFT-based sensitivity analysis provides a framework to investigate the sensitivity of the state variables to variations in input parameters. These parameters include the control inputs (actuation frequency and magnetic field strength), the parameters of the physical surroundings (viscosity and tissue stiffness), and the robot parameters (helix parameters, magnetic properties, and material). Following such a framework, considering the complexity of the magneto-elastic hydrodynamics in viscous fluids, is an important step to choose an optimal set of control inputs that yield a swimming behavior with minimal deviation from the prescribed trajectory.

It is also possible to combine the benefits of the sensitivity analysis and feedback control systems. The implementation of feedback control system capitalizes on directing the rotation axis of the helical robot toward a prescribed target using the orientation of the RPM as given by Equation (6). The position-dependent mapping, which maps the rotation axes of the RPM and the helical robot, is entirely dependent on position feedback. Below the step-out frequency, position of the helical robot is only needed as the orientation can be determined based on that of the RPM, then feedback control can be implemented on the joints of the serial manipulator. In this case, the sensitivity functions will provide optimal actuation variables and geometric features, whereas feedback will correct the swimming direction, enabling accurate robot trajectories.

If helical microrobots are to find biomedical and real world applications there is the possibility of moving between environments with heterogeneous rheological and structural properties. Nearly every location inside the human body can be accessed by bodily fluids. Therefore, transitions through the interface between two environments are likely to be required to navigate controllably inside a bodily fluid and then target a specific location. Consider, for example, a helical microrobot designed to restore the blood flow by drilling through the fibrin network of a thrombus that is inaccessible in a tethered fashion (current catheter-based clinical techniques cannot be used).[13] In this case, the microrobot can be inserted and controlled to swim toward the site of the thrombus for intervention by mechanical and/or chemical means. In either case, the helical microrobot would transduce the rotating magnetic field of the RPM into swimming in blood and screwing through the viscoelastic thrombus. This is an important medical application in which the microrobot may be required to transition between non-Newtonian and viscoelastic mediums, thereby providing access to peripheral vascular diseases that are inaccessible by catheter-based interventions. Note that the example described above represents helical propulsion in confined environments of fluid-filled lumen. In our model, the drag coefficients can be modified to account for the hydrodynamic interactions near walls by incorporating the influence of the medium gap between the robot and the wall. Note also that for the example described above, blood has non-Newtonian rheology and the dependence of its viscosity on the strain rate must be considered in the sensitivity analysis. However, there are several regions in which we can find a Newtonian–Viscoelastic interface in vivo. Nelson et al. has presented an extensive review with additional medical applications that involves moving through two mediums such as the urinary system and the prostate.[1] In these applications, the microrobot may transition from urine to soft-tissue environment in the kidney or the bladder to deploy localized therapies.

6. Conclusions

Controlled magnetic fields can be generated in such a manner, that the disturbances caused by variable input parameters in the physical surrounding do not yield relatively large deviation of the swimming path under open-loop action. On the basis of an RFT-based magneto-hydrodynamic model and global sensitivity analysis, we show that the low-frequency disturbance rejection is a result of the sensitivity of all the state variables that characterize helical propulsion to actuation frequency. In particular, when helical robot is actuated in low-*Re* flow using a single RPM, its states are more sensitive to variations in the actuation frequency than to variations in the separation distance between the magnet and the robot. This predicted behavior by the sensitivity analysis is compared with directly measured instantaneous states (positions and velocities) during helical propulsion between two fluids and actuation by two frequencies that are relatively close to one another. The presented framework is necessary to predict the input parameters that enable helical propulsion in a medium with unknown characteristics or in environments with varying parameters in time and space.

Acknowledgements

The authors would like to thank Mr. Ritwik Avaneesh for assistance with the development of the experimental setup and the motion control experiments. The authors would like to thank Dr. Michiel Warlé of the Department of Surgery at Radboud university medical center for many fruitful discussions and guidance on the medical applications of microrobots.

Conflict of Interest

The authors declare no conflict of interest.

Data Availability Statement

The data that support the findings of this study are available from the corresponding author upon reasonable request.

Keywords

helical propulsion, low-Reynolds numbers, magnetic, microrobots, resistive force theory, sensitivity analysis

Received: November 9, 2021
Revised: January 4, 2022
Published online:

[1] B. J. Nelson, I. K. Kaliakatsos, J. J. Abbott, *Annu. Rev. Biomed. Eng.* **2010**, *12*, 55.
[2] A. Darzi, Y. Munz, *Annu. Rev. Med.* **2004**, *55*, 223.
[3] J. Wang, W. Gao, *ACS Nano* **2012**, *6*, 5745.
[4] M. Sitti, H. Ceylan, W. Hu, J. Giltinan, M. Turan, S. Yim, E. Diller, *Proc. IEEE* **2015**, *103*, 205.
[5] A. Ghosh, P. Fischer, *Nano Lett.* **2009**, *9*, 2243.
[6] B. Sangwon, L. Jung-Min, P. Seung-Joon, L. Ahra, K. Kyo-in, P. Sunkil, P. Jaehong, C. Byoung-Doo, S. J. Mo, K. Kyung-ah, C. Hum, S. S. Young, J. Doyoung, D. Cho, *J. Micromech. Microeng.* **2005**, *15*, 6.
[7] S. Yim, E. Gultepe, D. H. Gracias, M. Sitti, *IEEE Trans. Biomed. Eng.* **2014**, *61*, 513.
[8] M. P. Kummer, J. J. Abbott, B. E. Kratochvil, R. Borer, A. Sengul, B. J. Nelson, *IEEE Trans. Rob.* **2010**, *25*, 6.
[9] C. K. Schmidt, M. Medina-Sánchez, R. J. Edmondson, O. G. Schmidt, *Nat. Commun.* **2020**, *11*, 5618.
[10] A. C. Hortelão, R. Carrascosa, N. Murillo-Cremaes, T. Patiño, S. Sánchez, *ACS Nano* **2019**, *13*, 429.
[11] O. Ergeneman, G. Chatzipirpiridis, J. Pokki, M. Marin-Suárez, G. A. Sotiriou, S. Medina-Rodriguez, J. F. F. Sanchez, A. Fernandez-Gutiérrez, S. Pane, B. J. Nelson, *IEEE Trans. Biomed. Eng.* **2012**, *59*, 3104.
[12] T. Patino, A. Porchetta, A. Jannasch, A. Lladó, T. Stumpp, E. Schäffer, F. Ricci, S. Sánchez, *Nano Lett.* **2019**, *19*, 6.
[13] I. S. M. Khalil, A. F. Tabak, K. Sadek, D. Mahdy, N. Hamdi, M. Sitti, *IEEE Rob. Autom. Lett.* **2017**, *2*, 927.
[14] S. Jeon, S. Kim, S. Ha, S. Lee1, E. Kim, S. Y. Kim, S. H. Park, J. H. Jeon, S. W. Kim, C. Moon, B. J. Nelson, J. young Kim, S.-W. Yu, H. Choi, *Int. J. Rob. Res.* **2019**, *4*, 30.
[15] F. Qiu, B. J. Nelson, *Engineering* **2015**, *1*, 021.
[16] J. J. Abbott, E. Diller, A. J. Petruska, *Annu. Rev. Control, Rob. Auton, Syst.* **2019**, *3*, 57.
[17] K. E. Peyer, L. Zhang, B. J. Nelson, *Nanoscale* **2013**, *5*, 1259.
[18] A. W. Mahoney, D. L. Cowan, K. M. Miller, J. J. Abbott, *2012 IEEE Int. Conf. on Robotics and Automation*, IEEE, Piscataway, NJ **2012**, pp. 3375–3380.
[19] T. W. R. Fountain, P. V. Kailat, J. J. Abbott, in *2010 IEEE Int. Conf. on Robotics and Automation*, IEEE, Piscataway, NJ **2010**, pp. 576–581.
[20] A. Hosney, A. Klingner, S. Misra, I. S. M. Khalil, in, *2015 IEEE/RSJ Int. Conf. on Intelligent Robots and Systems*, IEEE, Piscataway, NJ **2015**, pp. 1988–1993.
[21] B. Rodenborn, C.-H. Chen, H. L. Swinney, B. Liu, H. P. Zhang, *Proc. Natl. Acad. Sci. U. S. A.* **2013**, *110*, 5.
[22] J. Gray, G. J. Hancock, *J. Exp. Biol.* **1955**, *32*, 802.
[23] J. Lin, Z. Zhu, X. Jing, M. Lu, Y. Gu, *Adv. Theory Simul.* **2021**, *4*, 2100189.
[24] A. F. Tabak, *Adv. Theory Simul.* **2019**, *2*, 1800130.
[25] J. Tang, L. W. Rogowski, X. Zhang, M. J. Kim, *Nanoscale* **2020**, *12*.
[26] S. Gómez, F. A. Godínez, E. Lauga, R. Zenit, *J. Fluid Mech.* **2017**, *812*, 3.
[27] A. Barbot, D. Decanini, G. Hwang, *Int. J. Rob. Res.* **2020**, *39*, 4.
[28] J. L. Munch, D. Alizadehrad, S. B. Babu, H. Stark, *Soft Matter* **2016**, *12*.
[29] B. J. Nelson, K. E. Peyer, *ACS Nano* **2014**, *8*, 9.
[30] E. P. Furlani, *Permanent Magnet and Electromechanical Devices: Materials, Analysis, and Applications*, Academic Press, San Diego, CA **2009**.
[31] A. W. Mahoney, J. J. Abbott, in, *2012 4th IEEE RAS & EMBS International Conference on Biomedical Robotics and Biomechatronics (BioRob)*, IEEE, Piscataway, NJ **2012**, pp. 1632–1637.
[32] A. F. Tabak, *Adv. Theory Simul.* **2018**, *1*, 1700013.
[33] J. J. Abbott, K. E. Peyer, M. C. Lagomarsino, L. Zhang, L. Dong, I. K. Kaliakatsos, B. J. Nelson, *Int. J. Rob. Res.* **2009**, *28*, 11.
[34] I. S. M. Khalil, A. F. Tabak, K. Sadek, D. Mahdy, N. Hamdi, M. Sitti, *IEEE Rob. Autom. Lett.* **2017**, *2*, 927.
[35] N. D. Nelson, J. Delacenserie, J. J. Abbott, in *IEEE International Conference on Robotics and Automation (ICRA)*, IEEE, Piscataway, NJ **2013**, pp. 5372–5377.
[36] Y. C. Fung, N. Perrone, M. Anliker, *Biomechanics: Its Foundations and Objectives*, Prentice-Hall, Englewood Cliffs, NJ **1972**.
[37] A. W. Mahoney, N. D. Nelson, K. E. Peyer, B. J. Nelson, J. J. Abbott, *Appl. Phys. Lett.* **2014**, *104*, 144101.
[38] H. K. Khalil, *Nonlinear Systems*, 2nd Ed., Prentice Hall, New York **1996**.
[39] R. Avaneesh, R. Venezian, C.-S. Kim, J.-O. Park, S. Misra, I. S. M. Khalil, in *2021 IEEE/RSJ Int. Conf. on Intelligent Robots and Systems*, IEEE, Piscataway, NJ **2021**, pp. 8522–8527.
[40] D. Mahdy, A. Mohamed, A. Klingner, A. Tammam, A. Wahdan, M. Serry, I. S. M. Khalil, in *2017 IEEE Int. Conf. on Manipulation, Manufacturing and Measurement on the Nanoscale (3M-NANO)*, IEEE, Piscataway, NJ **2017**, pp. 319–322.
[41] J. Leclerc, H. Zhao, D. Bao, A. T. Becker, *IEEE Trans. Rob.* **2020**, *36*, 3.
[42] S. Tottori, L. Zhang, F. Qiu, K. k. Krawczyk, A. Franco-Obregõn, B. J. Nelson, *Adv. Mater.* **2012**, *24*, 6.
[43] S. Pane, V. Iacovacci, E. Sinibaldi, A. Menciassi, *Appl. Phys. Lett.* **2021**, *118*, 014102.
[44] G. T. van Moolenbroek, T. Patino, J. Llop, S. Sánchez, *Adv. Intell. Syst.* **2020**, *2*, 10.